# Spectral Broadening Effects on Pulsed-Source Digital Holography

Steven A. Owens, Mark F. Spencer, and Glen P. Perram

***Abstract*— Using a pulsed configuration, a digital-holographic system is setup in the off-axis image plane recording geometry, and spectral broadening via pseudo-random bit sequence is used to degrade the temporal coherence of the master-oscillator laser. The associated effects on the signal-to-noise ratio are then measured in terms of the ambiguity and coherence efficiencies. It is found that the ambiguity efficiency, which is a function of signal-reference pulse overlap, is not affected by the effects of spectral broadening. The coherence efficiency, on the other hand, is affected. As a result, the coherence efficiency, which is a function of effective fringe visibility, is shown to be a valid performance metric for pulsed-source digital holography.**

***Index Terms*— Digital holography, spatial heterodyne, coherent detection, coherence, signal-to-noise ratio, pulsed laser sources.**

## I. Introduction

FOR applications like long-range imaging, digital-holographic systems interfere a scattered signal with a strong reference to create a spatially modulated pattern known as a hologram [1]. This hologram is recorded digitally and processed computationally to estimate the complex-optical field, which in terms of the amplitude and wrapped phase contains information about the aberrations that exist along the propagation path [2], [3], [4]. In turn, digital holography robustly enables applications like long-range imaging [5], [6], [7], [8], [9], [10].

With applications like long-range imaging in mind, there are scenarios where the pathlength differences between the scattered signal and strong reference exceed the coherence length of the master-oscillator (MO) laser. These scenarios lead to limitations in the utility of digital-holographic systems, especially when the temporal coherence of the MO laser is degraded. To quantify these limitations, the signal-to-noise ratio (SNR) can be used to characterize system performance [11], [12]. In practice, there are several phenomena that lead to SNR loss, which are accounted for using component efficiencies that make up the total-system efficiency.

Recent experiments measured the total-system efficiency in terms of component efficiencies for a digital-holographic system in a continuous-wave (CW) configuration [13]. Here, it is assumed that both the scattered signal and the strong reference are derived from the same MO laser. Follow-on work then used the coherence efficiency to show that system performance degrades rapidly when the path-length difference between the scattered signal and strong reference exceeds the coherence length of the MO laser [14], [15]. Practically speaking, this outcome means that a CW configuration should not be used in such scenarios.

In lieu of a CW configuration, a pulsed configuration can be used to circumvent these aforementioned limitations. Here, it is assumed that both the signal pulse and the reference pulse are derived from the same MO laser. Recent experiments showed that when changing from a CW configuration to a pulsed configuration, the ambiguity efficiency needs to be introduced into the analysis to properly characterize system performance in terms of the SNR [16], [17]. In effect, the ambiguity efficiency accounts for the SNR loss due to nonideal signal-reference pulse overlap.

Of note, the experiments conducted in [16] used a homodyne-pulsed setup, whereas the experiments conducted in [17] used a heterodyne-pulsed setup. In the former, a postamplification beam splitter is used to create the signal and reference pulses from a single pulse train, whereas in the latter, a preamplification beam splitter is used to create the signal and reference pulses from two-independent pulse trains. As a result, the heterodyne-pulsed setup increases applicability, particularly for applications like long-range imaging. Such a setup readily allows for greater effective ranges, since the effective strengths of the signal and reference pulses can be set within the dynamic range of the camera, and the timing of each to be externally triggered to maximize signal-reference pulse overlap. Regardless of applicability, [16] and [17] ultimately showed that the total-system efficiency of both setups is consistent with one another (i.e., no new component efficiencies besides the ambiguity efficiency are required when switching from a homodyne- to a heterodyne-pulsed setup).

Moving forward it is also beneficial to characterize system performance as a function of degraded temporal coherence. In general, the temporal coherence of the MO laser may be degraded for either physics- or equipment-based reasons. Thus, understanding the effects of degraded temporal coherence helps in fully characterizing system performance in terms of the SNR.

In this paper, a heterodyne-pulsed setup is used to characterize the effects of degraded temporal coherence on pulsed-source digital holography. Specifically, spectral broadening via

Manuscript received 16 September 2022; revised 15 January 2023; accepted 17 February 2023. Date of publication 23 February 2023; date of current version 31 May 2023. *(Corresponding author: Steven A. Owens.)*

The authors are with the Department of Engineering Physics, Air Force Institute of Technology, Dayton, OH 45433 USA (e-mail: steven.owens.21@us.af.mil; mark.spencer@osamember.org; glen.perram@afit.edu).

Color versions of one or more figures in this article are available at https://doi.org/10.1109/JQE.2023.3248176.

Digital Object Identifier 10.1109/JQE.2023.3248176

pseudo-random bit sequence (PRBS) is used to degrade the temporal coherence of the MO laser. The results show that spectral broadening has no significant effect on the ambiguity efficiency, which is a function of signal-reference pulse overlap. However, the total-system efficiency is reduced in accordance with the coherence efficiency, which is a function of effective fringe visibility. While previously used to characterize system performance for a CW configuration [16], [17], this is the first time the coherence efficiency has been used to characterize system performance for a pulsed configuration. Therefore, the results presented in this paper are worth sharing in the peer-reviewed literature, as they provide an increased understanding of how degraded temporal coherence of the MO laser can lead to SNR loss in pulsed-source digital holography.

In what follows, Section II describes the theory needed to understand how spectral broadening via PRBS leads to degraded temporal coherence, as well as the efficiencies applicable to this paper. Section III then details the experiment, including the data-collection and data-processing methodologies. The results are presented in Section IV in terms of the ambiguity and coherence efficiencies. A conclusion follows in Section V.

## II. Theory

This section provides the background theory needed to interpret and analyze the results presented in Section IV. First, the relevant elements of spectral broadening via PRBS are introduced to provide insights into how the temporal coherence of the MO laser is degraded. Then, an overview of the applicable efficiencies, namely the ambiguity and coherence efficiencies, is given.

### A. Spectral Broadening via PRBS

Spectral broadening in this paper was achieved by phase modulating a MO laser via PRBS. In practice, PRBS involves a binary, randomly fluctuating electrical signal being driven into a phase modulator. In turn, the phase of the complex-optical field passing through the modulator is rapidly changed. Three factors, set by the user, characterize PRBS: (1) the pattern length, (2) the modulation frequency, and (3) the amplitude [18].

PRBS is pseudo-random because the length of the binary, or bit, sequence is finite before it repeats. This length, called the pattern length, is denoted as $2^{n_{PRBS}}-1$, where $n_{PRBS}$ is the shift register length used to create the pattern. The larger the $n_{PRBS}$, the longer the sequence is before the pattern repeats.

The modulation frequency is the number of possible phase changes per second. In practical terms, the temporal spacing between each bit, or the bit period, is determined by the modulation frequency. Together, the pattern length and modulation frequency drive the mode spacing in the phase-modulated spectrum, $\Delta\nu_{pms}$, of the complex-optical field [18]. In turn,

$$\Delta\nu_{pms} = \frac{\nu_{PRBS}}{2^{n_{PRBS}}-1}, \tag{1}$$

where $\nu_{PRBS}$ is the modulation frequency. If $n_{PRBS}$ is sufficiently large, the mode spacing will be such that the individual modes are non-resolvable, and the spectral line shape of the modulated laser source is broadened.

The amplitude of the PRBS signal, or peak-to-peak voltage, determines the magnitude of the phase change, known as the depth of modulation. This phase change leads to a change in instantaneous frequency, $\Delta\nu_{dm}$, of the complex-optical field [18]. As such,

$$\Delta\nu_{dm} = \frac{1}{2\pi}\frac{d\phi}{dt}, \tag{2}$$

where $\phi$ is the phase of the complex-optical field. With Eq. (2) in mind, a voltage setting of particular importance is referred to as the half-wave voltage. In general, the half-wave voltage results in a depth of modulation of $\pi$, leading to the greatest amount of broadening possible. Going beyond this depth of modulation will cause the line shape to narrow until it returns to the original line shape at a depth of modulation of $2\pi$.

Introducing PRBS will cause the linewidth of the MO laser to broaden with a sinc-squared line shape [19], [20]. The MO laser used for this paper has a Lorentzian line shape when not modulated by PRBS, resulting in a modulated line shape, $G$, of the form

$$G(\nu) = A_L\frac{\Delta\nu_L}{(\nu-\nu_0)^2+\left(\frac{\Delta\nu_L}{2}\right)^2} + A_S\ \mathrm{sinc}^2\left(\frac{\nu-\nu_0}{\Delta\nu_S}\right), \tag{3}$$

where $A_L$ and $A_S$ are the amplitudes of the Lorentzian and sinc-squared line shapes, respectively, $\Delta\nu_L$ and $\Delta\nu_S$ are the widths of the Lorentzian and sinc-squared line shapes, respectively, $\nu$ is the frequency, and $\nu_0$ is the center frequency of the line shapes. Here, $\mathrm{sinc}(x) = 1$ when $x = 0$ and $\mathrm{sinc}(x) = \sin(\pi x)/(\pi x)$ otherwise [21], [22].

Practically speaking, every phase modulator is different. Therefore, it is more accurate to measure the modulated line shapes and apply a fit using Eq. (3) than it is to estimate the modulated line shapes using PRBS characteristics. Doing so allows for the SNR loss to be measured as a function of (1) sinc-squared null location, $\Delta\nu_S$, related to PRBS frequency; and (2) the ratio of the energy in the sinc-squared line shape to the energy in the total line shape, or $\beta$, related to depth of modulation. When $\beta = 1$, the laser source is fully modulated, and the spectral-line shape is completely sinc-squared. Otherwise, the laser source is only partially modulated and exhibits both Lorentzian and sinc-squared line shapes.

### B. Efficiencies

This paper utilizes the off-axis image plane recording geometry (IPRG), creating a hologram in the image plane of a pupil by interfering a strong, off-axis, diverging reference pulse with a scattered, on-axis, converging signal pulse [2], [11]. The power definition of the SNR for this recording geometry is given by

$$SNR(x, y, \tau) = \eta_{tot}(x, y, \tau)\frac{4q_I^2}{\pi}\bar{m}_s(x, y), \tag{4}$$

where $(x, y)$ are the estimated image-plane coordinates, $\tau$ is the temporal delay between the centers of the reference and signal pulses, $\eta_{tot}$ is the total-system efficiency, $q_I$ is the image-plane sampling quotient, and $\bar{m}_S$ is the mean number of signal photoelectrons generated by the signal pulse.

Equation (4) assumes that the reference is sufficiently strong such that the digital-holographic system is operating in a shot-noise-limited regime [11], [23]. Any effects of the system not operating in the shot-noise limit are then captured by $\eta_{tot}$.

The goal of this paper is to analyze system performance in terms of the SNR as a function of degraded temporal coherence. Therefore, it is of interest to look closely at $\eta_{tot}$, as it is comprised of component efficiencies that account for SNR loss [13], [14], [16], [17]. Here,

$$\eta_{tot}(x, y, \tau) = \eta_{ern}\eta_{snl}(x, y)\,\eta_{pol}\eta_{mod}\eta_{amb}(\tau)\,\eta_{coh}(\tau), \tag{5}$$

where $\eta_{ern}$ is the excess-reference-noise efficiency, $\eta_{snl}$ is the shot-noise-limit efficiency, $\eta_{pol}$ is the polarization efficiency, $\eta_{mod}$ is the modulation efficiency, $\eta_{amb}$ is the ambiguity efficiency, and $\eta_{coh}$ is the coherence efficiency. The excess-reference-noise, shot-noise-limit, polarization, and modulation efficiencies are not dependent on the coherence of the pulses used to create the hologram [13], [24]. Because of this, these efficiencies are not of particular concern in this paper.

However, the ambiguity and coherence efficiencies are fundamentally linked to the temporal coherence of the pulses [16], [17], [25]. The ambiguity efficiency is derived from the zero-Doppler cut of the ambiguity function [17], [26], [27], such that

$$\eta_{amb}(\tau) = \left\langle \left| \int_{-\infty}^{\infty} U_R(x, y, t)\, U_S^*(x, y, t-\tau)\, dt \right|^2 \right\rangle, \tag{6}$$

where $U_R$ and $U_S$ are normalized complex-optical fields of the reference and signal pulses in the temporal domain, respectively, $t$ is time, $*$ denotes the complex conjugate, $|\cdot|^2$ is the square-magnitude operator, and $\langle\cdot\rangle$ is the spatial average operator. The square-magnitude operator is necessary in Eq. (6), as Eq. (4) uses the power definition of the SNR. On the other hand, the spatial average operator is not required in Eq. (6), but it is convenient to have spatially independent metrics when cross-evaluating multiple digital-holographic systems.

The coherence efficiency is a function of the effective complex degree of coherence, $\gamma_{eff}$, via the following relationship [14], [15]:

$$\eta_{coh}(\tau) = \left|\gamma_{eff}(\tau)\right|^2 \tag{7}$$

Put another way, $\eta_{coh}$ is related to the square of the effective fringe visibility. If the coherence length of the signal and reference pulses are much longer than the integration time of the imaging system and the pulses are identical, $\gamma_{eff}$ is equal to the complex degree of coherence, $\gamma$, of the MO laser. By the Wiener–Khinchin theorem, $\gamma_{eff}$ is then the inverse Fourier transform of the normalized laser spectral line shape [28].

Building on the CW formulation contained in [14] and [15], $\gamma_{eff}$ requires further calculation and will be dependent on the specific pulse-generation process used in the experiment. For the experiment described in Section III, signal and reference pulses are independently carved out from a phase-modulated MO laser, resulting in a heterodyne-pulsed configuration. Therefore, the calculation of $\gamma_{eff}$ begins with carving out a section of $\gamma$ of the phase-modulated MO laser, such that

$$\gamma_{S,R}(t) = \gamma(t)\, T_{S,R}(t), \tag{8}$$

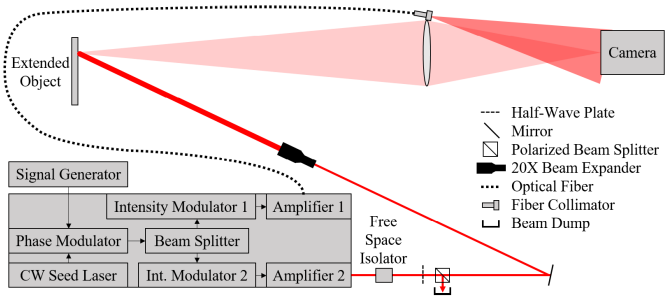


Fig. 1. Experimental setup.

where $\gamma_S$ and $\gamma_R$ are analogous to the complex degrees of coherence of the signal and reference pulses, respectively, and $T_S$ and $T_R$ are the temporal profiles of the signal and reference pulses, respectively. Both $\gamma$ and $T_{S,R}$ equal unity at $t = 0$ and are less otherwise. Note that Eq. (8) assumes any amplification subsequent to pulse carving does not affect the complex degree of coherence. Because the pulses may be delayed in relation to one another, $\gamma_{eff}$ is found via the correlation of the square roots of $\gamma_R$ and $\gamma_S$, viz.

$$\gamma_{eff}(\tau) = \int_{-\infty}^{\infty} \sqrt{\gamma_R(t)}\,\sqrt{\gamma_S(t-\tau)}\,dt. \tag{9}$$

## III. Experiment

The experimental setup is shown in Fig. 1. Using a master oscillator power amplifier, or MOPA, configuration, two-independent pulse trains were generated by a custom-built NP Photonics Coherent High Energy Pulsed Fiber Laser System [29]. In practice, other heterodyne-pulsed setups exist (e.g., via Q-switching, mode locking, etc.) but the conclusions reached in this paper hold for them as well. They also hold for homodyne-pulsed setups, which use a single pulse train.

As shown in Fig. 1, a 1064 nm CW seed laser was used as the MO laser to create a digital-holographic system in the off-axis IPRG with a short-wave infrared (SWIR) camera The output of the CW seed laser was passed through a fiber-coupled phase modulator controlled by an external signal generator. After the phase modulator, two-independent beam trains were created by a beam splitter. Intensity modulators and ytterbium-doped fiber amplifier stages were then used to carve out and amplify two-independent pulse trains, respectively. Both pulse trains operated at a 1 kHz repetition rate.

Pulse train 1 generated 8.8 ns reference pulses with an average energy of 10 nJ, which exited the backend tip of a 2 m long polarization-maintaining, single-mode optical fiber. The backend tip was coupled to an adjustable collimator to maintain a nearly uniform energy distribution over the focal-plane array (FPA) of the camera while ensuring enough reference energy was captured. This collimator was placed off-axis next to the imaging lens and tilted toward the camera.

Pulse train 2 produced 10 ns signal pulses with an average energy of 10 $\mu$J. These pulses were passed through a free-space isolator, half-wave plate, and polarized beam splitter (PBS) to control the energy of the signal pulses. The pulses were then sent through a 20x beam expander, scattered off a sheet of Labsphere Spectralon (i.e., a stationary, optically

rough, extended object) with a vendor-specified 99% Lambertian reflectivity. This reflected light was imaged onto the camera via a 2.54 cm imaging lens. Of note, the object and image distances of the imaging system were set such that the measured image-plane sampling quotient, $q_I$, was 3.35. By definition, $q_I$ represents the number of circular-pupil diameters that can fit across the Fourier plane [2], [11].

The average energy of the pulses from both pulse trains fluctuated ±16% pulse to pulse over a 6-hour time period, much longer than what was required to collect any single dataset. Therefore, the energy in each pulse train was considered stable. A Berkeley Nucleonics Corporation Model 577 Digital Delay/Pulse Generator was used to control the temporal delay, $\tau$, between the signal and reference pulses. This pulse generator provided a minimum sampling resolution of 250 ps and a root-mean-squared jitter of 100 ps.

A Picosecond Pulse Labs Model 12020 Pulse/Pattern Generator was used to control the fiber-coupled phase modulator. This pattern generator provided shift register lengths of $5 \leq n_{PRBS} \leq 31$, modulation frequencies of 15 MHz $\leq \nu_{PRBS} \leq$ 1 GHz, and peak-to-peak voltages of 55 mV $\leq V_{p-p} \leq$ 2.5 V. The fiber-coupled phase modulator restricted the maximum $V_{p-p}$ to 300 mV. Additionally, due to laser-system constraints, these peak-to-peak voltages could not be converted into their associated depths of phase modulation. Therefore, $\beta$ was measured from the phase-modulated CW spectral line shapes and used as a proxy for the depth of modulation.

For the camera, an Allied Vision Goldeye G-033 SWIR TEC1 was used with a pixel-well depth of 25,000 photoelectrons (pe) and a quantum efficiency of 77% at 1064 nm. This camera had an unstable gain region for integration times less than 25 $\mu s$. As a result, over a quarter of the pixel-well depth was filled by dark-current noise, making dark-current noise the dominant factor in the camera-noise variance, $\sigma_n^2$. Overall, $\sigma_n^2 = 6,486$ pe$^2$. Due to the unstable gain region, both pulses were set to arrive at the FPA of the camera near the 27 $\mu s$ integration-time mark with a total frame-integration time of 30 $\mu s$.

To avoid camera-pixel saturation while still maximizing sensing, the mean number of photoelectrons generated by the signal and reference at the camera, $\bar{m}_S$and $\bar{m}_R$ respectively, were set such that $\bar{m}_S = 85$ pe and $\bar{m}_R = 11,121$ pe. Assuming Poisson statistics, where the mean equals the variance, these set values meant that the reference noise did not dominate all other noise sources, as $\sigma_n^2 > 1/2\bar{m}_R$. Therefore, the digital-holographic system used in this experiment was not operating in the shot-noise-limited regime [11], [23]. However, this outcome did not affect the ambiguity and coherence efficiencies and is accounted for by other independent efficiencies within the total-system efficiency [16], [17], [25].

### A. Data-Collection Methodology

This experiment was performed in two separate parts. The first part of the experiment focused on the ambiguity efficiency. Three datasets were collected, each corresponding to a different set of PRBS parameters. The first dataset was used as a baseline; therefore, the PRBS generator was disabled. Then, two datasets were taken with the following parameters: (1) $\nu_{PRBS} = 15$ MHz, $V_{p-p} = 200$ mV; and (2) $\nu_{PRBS} = 1$ GHz, $V_{p-p} = 75$ mV. For these two datasets, the shift register length was set to the maximum possible value, $n_{PRBS} = 31$. This choice guaranteed the minimal-mode spacing for all PRBS frequencies [see Eq. (1)].

For each dataset, digital holograms were collected for temporal delay values from $\tau$ = -6 ns to +6 ns in 1 ns increments and from $\tau$ = -2 ns to +2 ns in 0.25 ns increments to sufficiently sample both the wings and the peak of the ambiguity efficiency curve. Two measurements were taken at $\tau = 0$ ns, one at the beginning of the overall data collection period and one at the halfway mark, to ensure that the master oscillator and amplification paths were performing consistently for the entire dataset. For each increment of $\tau$, the Labsphere Spectralon sheet was rotated to generate 10 distinct speckle realizations. For each speckle realization, 10 digital-hologram frames were collected for a total of 100 digital-hologram frames for each temporal pulse delay value. This was done for averaging during data processing. Additionally, 10 reference-only frames and 10 signal-only frames were collected for each speckle realization during both $\tau = 0$ ns measurements. Reference-only and signal-only frames were unnecessary for all temporal delay values because the energy of both pulse trains was stable for each individual dataset. After all other frames in the dataset were collected, 100 background frames were collected so that the background and camera noise could be appropriately accounted for during efficiency calculations.

After processing and analyzing the data from the first part of the experiment (as described in Section III.B), the data-collection methodology changed. Results from the first experiment showed the ambiguity efficiency was not significantly affected by the PRBS signal. However, the total-system efficiency was affected uniformly by a constant multiplier. Therefore, the coherence efficiency at a single value of $\tau$ was sufficient to characterize the coherence efficiency for all pulse delay values. As such, digital holograms were only taken at $\tau = 0$ ns for various modulation frequency and peak-to-peak voltage pairings. Those pairings can be grouped as follows:

(1) a baseline for which PRBS was disabled;
(2) stepping from $V_{p-p} = 100$ mV to $V_{p-p} = 300$ mV in 50 mV increments, with an additional collection at $V_{p-p} = 55$ mV, while holding $\nu_{PRBS} = 100$ MHz; and
(3) stepping from $\nu_{PRBS} = 15$ MHz to $\nu_{PRBS} = 90$ MHz in 15 MHz increments, from $\nu_{PRBS} = 100$ MHz to $\nu_{PRBS} = 145$ MHz in 15 MHz increments, and from $\nu_{PRBS} = 200$ MHz to $\nu_{PRBS} = 300$ MHz in 50 MHz increments while holding $V_{p-p} = 200$ mV.

The second grouping was collected to characterize the coherence efficiency in terms of the depth of modulation. The third grouping was collected to characterize the coherence efficiency in terms of the modulation frequency. As with the first part of the experiment, the shift register length was set such that $n_{PRBS} = 31$ for all pairings.

For each modulation frequency and peak-to-peak voltage pairing, the digital-hologram collection process followed that of the first part of this experiment (i.e., 10 speckle realizations,

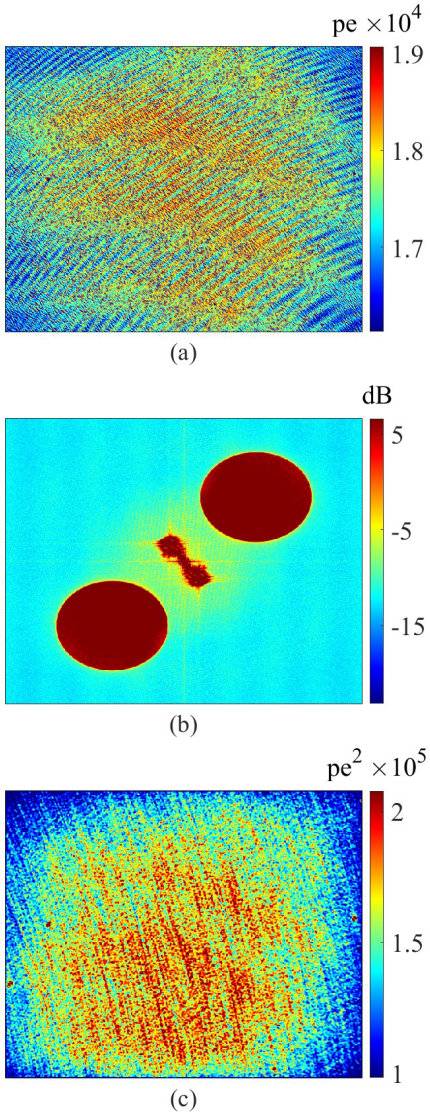


Fig. 2. An example of frame-demodulation process involving (a) a real–valued, digital-hologram frame, (b) the associated square-magnitude of the complex-valued Fourier plane, and (c) the associated square-magnitude of the complex-valued image plane.

with 10 digital-hologram frames per speckle realization). Additionally, 10 reference-only frames and 10 signal-only frames were collected for each speckle realization for the baseline. As a reminder, the energy of both pulse trains was considered stable so reference-only and signal-only frames were not necessary for each pairing. After data for all pairings were collected, 100 background frames were collected so the background and camera noise could be accounted for during the calculations. All frames from both parts of the experiment were imported to MATLAB for processing.

### *B. Data-Processing Methodology*

To calculate the ambiguity and coherence efficiencies, the collected digital-hologram frames were demodulated. An example of this frame-demodulation process is shown in Fig. 2.

The frame-demodulation process consisted of taking a discrete inverse Fourier transform on a real-valued, digital-hologram frame, as shown in Fig. 2(a), to obtain the associated complex-valued Fourier plane, the square-magnitude of which is shown in Fig. 2(b). In accordance with the off-axis IPRG [2], [11], the Fourier plane contained four key terms:

(1) The signal field (the data in the top-right circular pupil),
(2) The complex-conjugate of the signal field (the data in the bottom-left circular pupil),
(3) The local-oscillator-autocorrelation term (the non-circularly symmetric data centered at DC), and
(4) The pupil-autocorrelation term (the circularly symmetric data centered at DC).

With (1)-(4) in mind, a pupil-filter function was used to filter the signal field. The filtered signal field was then centered in the Fourier plane before a discrete Fourier transform was applied to obtain the associated complex-valued image plane. Finally, the square-magnitude was calculated in units of $\text{pe}^2$, to obtain a demodulated energy frame, as shown in Fig. 2(c). This last step was done in accordance with the power definition of the SNR [see Eq. (4)] and concluded the frame-demodulation process.

All of the collected digital-hologram frames underwent this frame-demodulation process individually. In turn, the 100 demodulated energy frames associated with a specific pulse delay, $\tau$, were averaged together to calculate the mean demodulated energy at that $\tau$. This process was repeated for all pulse-delay values. The frame-demodulation process and the mean demodulated energy calculation were repeated for the collected reference-only, signal-only, and background frames using the same pupil filter used for the digital-hologram frames, ensuring that noise was appropriately accounted for during the efficiency calculations. It is important to note that averaging before the collected digital-holography frames were demodulated would have effectively reduced the SNR, as there was a piston phase mismatch introduced between the signal and reference pulses on a frame-to-frame basis.

From the mean demodulated energy, the measured ambiguity efficiency, $\eta'_{amb}$, was computed using the following relationships:

$$E'_N(x,y) = E'_{D-S}(x,y) + E'_{D-R}(x,y) - E'_{D-B}(x,y), \tag{10}$$

$$E'_H(x,y,\tau) = E'_{D-H}(x,y,\tau) - E'_N(x,y), \tag{11}$$

$$\eta'_{tot}(\tau) = \left\langle \frac{SNR'(x,y,\tau)}{SNR(x,y)} \right\rangle = \frac{\pi}{4q_I^2} \left\langle \frac{E'_H(x,y,\tau)/E'_N(x,y)}{\bar{m}'_S(x,y) - \bar{m}'_B(x,y)} \right\rangle, \tag{12}$$

and

$$\eta'_{amb}(\tau) = \frac{\eta'_{tot}(\tau)}{\eta'_{tot}(0)}, \tag{13}$$

where $E'_N$ is the measured noise energy; $E'_{D-S}$, $E'_{D-R}$, and $E'_{D-B}$ are the measured signal, reference, and background average energies after demodulation, respectively; $E'_H$ is the measured hologram energy; $E'_{D-H}$ is the measured hologram

average energy after demodulation, $SNR'$ is the measured SNR; and $\bar{m}'_S$ and $\bar{m}'_B$ are the measured mean number of signal and background photoelectrons generated, respectively. Note that the substantial dark-current noise from the camera is accounted for with $\bar{m}'_B$ and $E'_{D-B}$ and is removed, where applicable, by background subtraction. It should also be noted that the $\pi/4\, q_I^2$ term in Eq. (12) is necessary to account for the ratio of the pupil-filter area to the Fourier-plane area [2], [11].

The measured coherence efficiency, $\eta'_{coh}$, was calculated in a similar fashion, such that

$$\eta'_{coh}(\beta, \Delta\nu_S) = \frac{\eta'_{tot}(\beta, \Delta\nu_S)}{\eta'_{tot}(0, 0)}, \tag{14}$$

where $\beta$ and $\Delta\nu_S$ were estimated from the phase-modulated MO laser spectral line shapes [see Eq. (3)]. The phase-modulated pulsed source spectral line shapes were not used as accurately capturing such spectra was not possible with the available equipment [17]. Therefore, some error between the theoretical coherence efficiency, calculated using Eqs. (7) and (9), and the measured coherence efficiency was expected. Also, because all coherence efficiency measurements were taken at $\tau = 0$ ns, the dependence on $\tau$ was dropped from Eq. (14).

## IV. Results and Discussion

The effects of spectral broadening on the ambiguity efficiency were analyzed by systematically degrading the temporal coherence of the MO laser, then calculating the resulting ambiguity efficiencies using Eqs. (10)-(13). Comparison of these measured ambiguity efficiencies showed that spectral broadening via PRBS did not significantly affect the ambiguity efficiency. However, preliminary analysis showed that degraded temporal coherence of the MO laser did reduce the total-system efficiency in a nearly uniform manner. Therefore, a deeper investigation was performed. This analysis showed that the coherence efficiency was appropriate to characterize these effects.

### A. Ambiguity Efficiency Analysis

The phase-modulated MO laser line shapes associated with the three datasets collected during the first part of this experiment (see Section III.A) are shown in Fig. 3. These line shapes, as well as all line shapes used in this paper, were measured using a using a Thorlabs SA200-8B scanning Fabry-Perot interferometer with a 7.5 MHz resolution. Alongside these line shapes are the ambiguity efficiencies calculated using Eq. (13) for the same three datasets.

As seen in Fig. 3(b), the ambiguity efficiencies follow the same general shape regardless of modulation frequency or peak-to-peak voltage. At first glance, this result is seemingly in contradiction with the phase-modulated MO laser line shapes shown in Fig. 3(a). In Fig. 3(a), the energy in the peak is distributed to the wings as a function of amount of temporal degradation. In other words, more broadening occurs for greater values of $\nu_{PRBS}$ and $V_{p-p}$. This last point is most readily visible for the $\nu_{PRBS} = 15$ MHz, $V_{p-p} = 200$ mV case, where the peak power is roughly 36% of the baseline

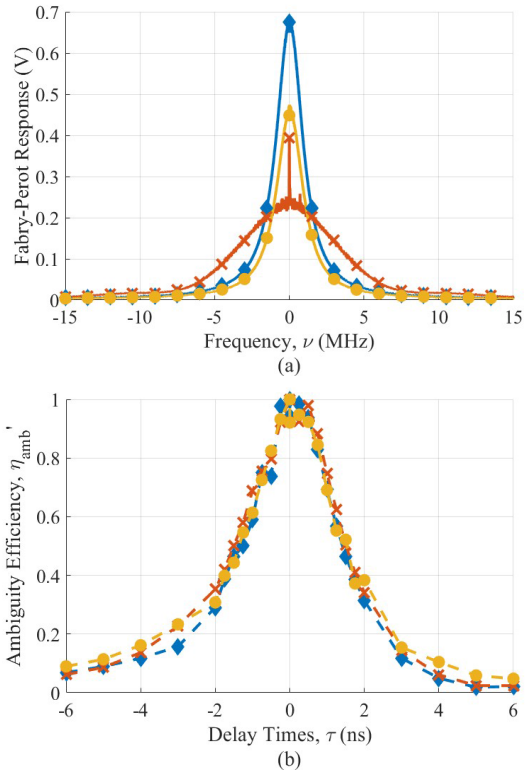


Fig. 3. Comparing the (a) phase-modulated MO laser line shapes and (b) ambiguity efficiencies for the following $\nu_{PRBS}$ and $V_{p-p}$ pairings: $\nu_{PRBS} = 0$ MHz, $V_{p-p} = 0$ mV (−♦); $\nu_{PRBS} = 15$ MHz, $V_{p-p} = 200$ mV (−×); and $\nu_{PRBS} = 1$ GHz, $V_{p-p} = 75$ mV (−•).

($\nu_{PRBS} = 0$ MHz, $V_{p-p} = 0$ mV) but has significantly more energy in the wings.

The degradation of the MO laser seen in Fig. 3(a) may bring about the expectation of system performance falling off faster as the temporal delay between the pulses increases (i.e., a narrower ambiguity efficiency). However, this expectation must be tempered by the heterodyne nature of the digital-holographic system. By definition, the reference and signal pulses of a heterodyne-pulsed setup have non-identical temporal phase characteristics. This difference in temporal phase determines the location of the hologram nulls [17]. As phase modulation is introduced into each pulse independently, the difference in temporal phase between the pulses changes as function of time. Therefore, the hologram null locations are also changing as a function of time, partially washing out the recorded hologram fringes for all values of $\tau$. Because this is a uniform effect for all $\tau$, the ambiguity efficiency was not affected, and the results shown in Fig. 3(b) are not in contradiction with the phase-modulated line shapes.

Another way to reach the same conclusion is to look at the PRBS noise characteristics. Because $n_{PRBS} > 20$, the noise characteristics associated with the PRBS signals used in this experiment were approximately Gaussian [30]. The mean of a Gaussian-noise distribution is zero. Therefore, by using the mean demodulated energy for the ambiguity-efficiency calculations, the spectral variance of the individual hologram frames was averaged out. This outcome, paired with the non-deterministically correlated phase content of the reference and

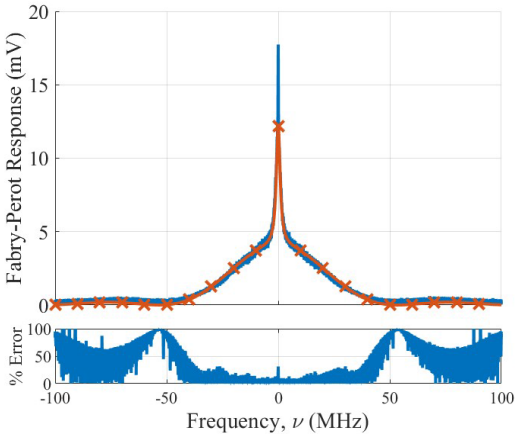


Fig. 4. Phase-modulated MO laser line shape (–) with a fitted line shape (−×). The absolute percent error of the fit is plotted underneath.

signal pulses (a key feature of heterodyne-pulsed setups), means that no change in the ambiguity efficiency should be expected. Fig. 3(b) validates this claim.

It was concluded from Fig. 3 that degrading the temporal coherence of the MO laser did not significantly affect the ambiguity efficiency of a digital-holographic system with a heterodyne-pulsed setup.

### B. Coherence Efficiency Analysis

While the ambiguity efficiency was not significantly changed as a function of degraded temporal coherence of the MO laser, preliminary results showed that the total-system efficiency was affected. Therefore, the coherence efficiency was introduced to account for these effects. The coherence efficiency was predicted using Eqs. (7)-(9) with an estimated complex degree of coherence calculated from fitting the phase-modulated MO laser line shape with Eq. (3). An example of this fit is shown in Fig. 4.

To create the fitted line shape in Fig. 4, the Lorentzian fit was given infinite weight near the center of the line shape and the sinc-squared fit was given infinite weight in the wings. These weights ensured that the unmodulated and modulated sections, respectively, of the line shape were fit as accurately as possible. Nonetheless, a narrow peak on the order of kHz in width and centered on the origin was not captured well by the Lorentzian fit. This narrow, poorly captured peak appeared in all of the line-shape fits except the unmodulated baseline, indicating there was a systematic, structured element unaccounted for in the phase-modulated line shapes. However, the percent error over this poorly captured peak was significantly less than the error at the sinc-squared null locations and further out in the wings. Note that a more-complicated line shape was fit to the measured phase-modulated MO laser data to account for this narrow peak, but the effect on the coherence efficiency characterization was negligible. It should also be noted that the kHz linewidth was orders of magnitude narrower than the resolution of the Fabry-Perot interferometer used to measure the spectra. With all three of these factors in mind, this peak was ignored, and the summation of a Lorentzian and sinc-squared line shape [see Eq. (3)] was simply used as the fit equation.

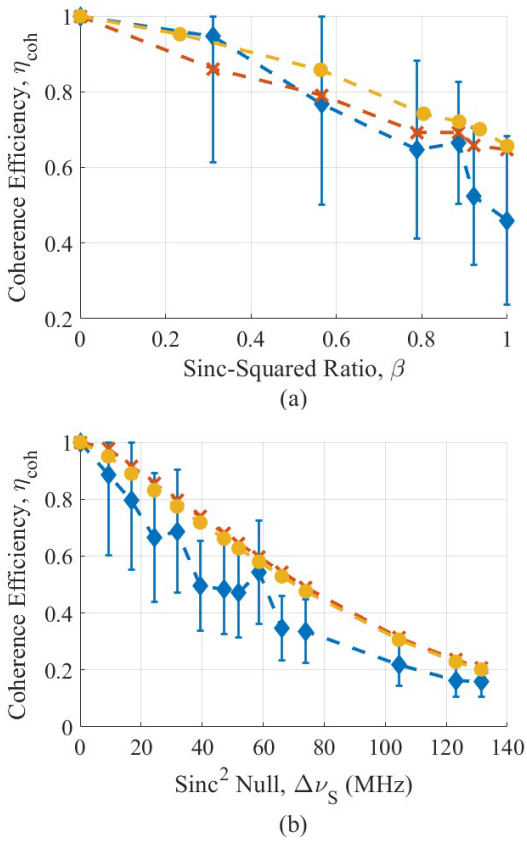


Fig. 5. Measured coherence efficiency (- ♦) and associated uncertainty as (a) $v_{PRBS}$ is held at 100 MHz and (b) $V_{p-p}$ is held to 200 mV. In (a), the theoretical coherence efficiency was calculated using the infinite weighting method (−×) and without weights (−•). In (b), the theoretical curves were calculated for the $\beta$-fit values (−×) and for $\beta = 1$ (−•).

From the fits, values for $\beta$ and $\Delta\nu_S$ were calculated for use during coherence efficiency characterization. The coherence efficiency, as calculated using Eq. (14), is shown in Fig. 5.

For Fig. 5(a), a PRBS frequency of 100 MHz was held constant as the input peak-to-peak voltage changed. This allowed the coherence efficiency to be characterized as a function of the depth of modulation using $\beta$ as a stand-in variable. Alongside the measured data curve are two theoretical curves calculated using Eq. (7). One theoretical curve was generated using the infinite-weighting method described for Fig. 4. The other theoretical curve fit Eq. (3) directly to the phase-modulated MO laser line shapes with no weighting method. As can be seen in Fig. 5(a), the infinite-weighting method was the more accurate method for $\beta > 0.5$ and followed the shape of the measured curve relatively well over the same region. The non-weighted theoretical curve was more accurate for $\beta < 0.4$ and followed the measured curve shape well over that region. However, neither theoretical curve predicted the entire measured curve well. This outcome indicated that the coherence efficiency, as presented in Eq. (7), is sensitive to minor changes in the input and a slightly more accurate model for the effective complex degree of coherence would lead to a more accurate prediction.

Fig. 5(b) shows the measured coherence efficiency as a function of PRBS frequency while the input peak-to-peak voltage was held at 200 mV. This input voltage was used as it was near the half-wave voltage of the phase modulator. Therefore, the sinc-squared portion of the phase-modulated MO laser line shape was maximized, and the locations of the sinc-squared nulls were as evident as possible. This outcome allowed the coherence efficiency to be characterized as a function of modulation frequency using $\Delta\nu_S$ as a stand-in variable.

As with Fig. 5(a), two theoretical curves are presented along with the measured data in Fig. 5(b). One theoretical curve used the $\beta$ values calculated from the infinitely weighted line fits and the other substituted those values with $\beta = 1$ (i.e., assumed maximum modulation). Both theoretical curves matched the shape of the measured data curve and relatively matched the magnitude, although both predictions were slightly greater. The $\beta = 1$ curve had lower magnitudes at all modulation frequencies. This outcome was a positive indication as an increased depth of modulation should, and did, lead to a decrease in the theoretical coherence efficiency.

The higher-magnitude theoretical curves in Figs. 5(a) and 5(b) were not unexpected. As mentioned in Section III.B, the values for $\beta$ and $\Delta\nu_S$ were calculated from the fit equations for the phase-modulated MO laser line shapes, not the phase-modulated pulsed source line shapes. Recording phase-modulated pulsed spectra is non-trivial and was not possible with the available equipment. Also, from previous experiments [14], [15], it was known that the fiber-amplifier stages used in this experiment significantly changed the spectral line shape from that of the MO laser. In practice, these stages introduced at least one additional longitudinal mode. Therefore, accurate approximations for the reference and signal spectral line shapes could not have been made. Despite this shortcoming, relatively accurate predicted coherence efficiency curves were produced. This outcome indicated that the coherence efficiency, as detailed in Section II, was valid and appropriate to characterize the performance of a digital-holographic system with a heterodyne-pulsed setup, particularly as a function of degraded temporal coherence of the MO laser.

### C. Discussion

While the motivation for this paper focused on the practicalities of using digital-holographic systems for applications like long-range imaging, there is still a need to further characterize the ambiguity efficiency in terms of degraded temporal coherence. As such, future pulsed-source digital holography experiments should look at the ambiguity efficiency as a function of PRBS bit alignment.

If the bit sequences of the reference and signal pulses are perfectly aligned, the ambiguity efficiency should be greater than when the sequences are misaligned. There are two potential experiments capable of analyzing this relationship. One involves using the homodyne-pulsed configuration and very accurate and precise path-length differences. On average, this experiment should lead to a narrow spike in ambiguity efficiency at $\tau = 0$ ns with no other changes.

The second experiment involves fine-tuning the MO laser phase modulation. With sufficient control, the bits of the modulation sequence could be consistently overlapped as desired. This experiment would lead to perfect bit overlap at any desired amount of pulse overlap. It would also enable measurement of the desired efficiencies when the bit sequence of the pulses was exactly one bit off, two bits off, etc.

## V. Conclusion

In this paper, spectral broadening via pseudo-random bit sequence was used to degrade the temporal coherence of a MO laser. This MO laser was then used to create a digital-holographic system with a heterodyne-pulsed setup. The associated effects on the SNR were measured in terms of the ambiguity and coherence efficiencies. It was found that the ambiguity efficiency, which is a function of signal-reference pulse overlap, was not affected by the effects of spectral broadening. The coherence efficiency, on the other hand, was affected. As a result, the coherence efficiency, which is a function of effective fringe visibility, was shown to be a valid performance metric for pulsed-source digital holography.

## References


[1] J. W. Goodman and R. W. Lawrence, "Digital image formation from electronically detected holograms," *Appl. Phys. Lett.*, vol. 11, no. 3, pp. 77–79, May 1967.

[2] M. F. Spencer, R. A. Raynor, M. T. Banet, and D. K. Marker, "Deep-turbulence wavefront sensing using digital-holographic detection in the off-axis image plane recording geometry," *Opt. Eng.*, vol. 56, no. 3, Oct. 2016, Art. no. 031213.

[3] M. T. Banet, M. F. Spencer, and R. A. Raynor, "Digital-holographic detection in the off-axis pupil plane recording geometry for deep-turbulence wavefront sensing," *Appl. Opt.* vol. 57, no. 3, pp. 465–475, 2018.

[4] D. E. Thornton, M. F. Spencer, and G. P. Perram, "Deep-turbulence wavefront sensing using digital holography in the on-axis phase shifting recording geometry with comparisons to the self-referencing interferometer," *Appl. Opt.*, vol. 58, no. 5, pp. A179–A189, Feb. 2019.

[5] S. T. Thurman and J. R. Fienup, "Correction of anisoplanatic phase errors in digital holography," *J. Opt. Soc. Amer. A, Opt. Image Sci.*, vol. 25, no. 4, pp. 995–999, 2008.

[6] J. C. Marron, R. L. Kendrick, N. Seldomridge, T. D. Grow, and T. A. Höft, "Atmospheric turbulence correction using digital holographic detection: Experimental results," *Opt. Exp.*, vol. 17, no. 14, pp. 11638–11651, 2009.

[7] A. E. Tippie and J. R. Fienup, "Phase-error correction for multiple planes using a sharpness metric," *Opt. Lett.*, vol. 34, no. 5, pp. 701–703, 2009.

[8] A. E. Tippie and J. R. Fienup, "Multiple-plane anisoplanatic phase correction in a laboratory digital holography experiment," *Opt. Lett.*, vol. 35, no. 19, pp. 3291–3293, 2010.

[9] C. J. Pellizzari, M. F. Spencer, and C. A. Bouman, "Imaging through distributed-volume aberrations using single-shot digital holography," *J. Opt. Soc. Amer. A, Opt. Image Sci.*, vol. 36, no. 2, pp. A20–A33, Feb. 2019.

[10] C. J. Radosevich, C. J. Pellizzari, S. Horst, and M. F. Spencer, "Imaging through deep turbulence using single-shot digital holography data," *Opt. Exp.*, vol. 28, no. 13, pp. 19390–19401, 2020.

[11] M. F. Spencer, "Spatial heterodyne," in *Encyclopedia of Modern Optics*, 2nd ed., B. Guenther and D. Steel, Eds. Amsterdam, The Netherlands: Elsevier, 2018.

[12] M. F. Spencer and D. E. Thornton, "Signal-to-noise models for digital-holographic detection," *Proc. SPIE*, vol. 10650, May 2018, Art. no. 1065008.

[13] D. E. Thornton, M. F. Spencer, C. A. Rice, and G. P. Perram, "Digital holography efficiency measurements with excess noise," *Appl. Opt.*, vol. 58, no. 34, pp. G19–G30, Dec. 2019.

[14] D. E. Thornton, D. Mao, M. F. Spencer, C. A. Rice, and G. P. Perram, "Digital holography experiments with degraded temporal coherence," *Opt. Eng.*, vol. 59, no. 10, p. 1, Jan. 2020.

[15] D. E. Thornton, M. F. Spencer, C. A. Rice, and G. P. Perram, "Impacts of laboratory vibrations and laser flicker noise on digital holography," *IEEE J. Quantum Electron.*, vol. 56, no. 5, Oct. 2020, Art. no. 1400107.
[16] S. A. Owens, M. F. Spencer, D. E. Thornton, and G. P. Perram, "Pulsed laser source digital holography efficiency measurements," *Appl. Opt.*, vol. 61, no. 16, pp. 4823–4832, 2022.
[17] S. A. Owens, M. F. Spencer, and G. P. Perram, "Digital-holography efficiency measurements using a heterodyne-pulsed configuration," *Opt. Eng.*, vol. 61, no. 12, Dec. 2022, Art. no. 123101.
[18] C. Zeringue, I. Dajani, S. Naderi, G. T. Moore, and C. Robin, "A theoretical study of transient stimulated Brillouin scattering in optical fibers seeded with phase-modulated light," *Opt. Exp.*, vol. 20, no. 19, pp. 21196–21213, Sep. 2012.
[19] A. Flores, C. Robin, A. Lanari, and I. Dajani, "Pseudo-random binary sequence phase modulation for narrow linewidth, kilowatt, monolithic fiber amplifiers," *Opt. Exp.*, vol. 22, no. 15, pp. 17735–17744, 2014.
[20] B. Anderson, A. Flores, R. Holten, and I. Dajani, "Comparison of phase modulation schemes for coherently combined fiber amplifiers," *Opt. Exp.*, vol. 23, no. 21, pp. 27046–27060, 2015.
[21] A. E. Siegman, "Why the sinc function should be defined as (sinx)/x and not $(\sin\pi x/\pi x)$," *Appl. Opt.*, vol. 13, no. 4, pp. 705–706, 1974.
[22] W. H. Steel, "Why the sinc function should be defined as (sinx)/x and not $(\sin\pi x/\pi x)$ comments," *Appl. Opt.*, vol. 13, no. 8, p. 1734, Aug. 1974.
[23] D. E. Thornton, C. J. Radosevich, S. Horst, and M. F. Spencer, "Achieving the shot-noise limit using experimental multi-shot digital holography data," *Opt. Exp.*, vol. 29, no. 6, pp. 9599–9617, 2021.
[24] D. E. Thornton, M. T. Banet, and M. F. Spencer, "Subaperture sampling for digital-holography applications involving atmospheric turbulence," *Appl. Opt.*, vol. 60, no. 25, pp. G30–G39, Sep. 2021.
[25] S. A. Owens, M. F. Spencer, and G. P. Perram, "Complex phase effects on a pulsed-source digital holography system," *Proc. SPIE*, vol. 12092, May 2022, Art. no. 1209206.
[26] P. M. Woodward, *Probability and Information Theory with Applications to Radar*. Norwood, MA, USA: Artech House, 1980.
[27] N. Levanon and E. Mozeson, *Radar Signals*. Hoboken, NJ, USA: Wiley, 2004.
[28] J. W. Goodman, *Statistical Optics*, 2nd ed. Hoboken, NJ, USA: Wiley, 2015.
[29] *Coherent High Energy Pulsed Fiber Laser System (CHELS) Product User Manual (6000456)*, NP Photon., Tucson, AZ, USA, 2020.
[30] E. D. Lipson, K. W. Foster, and M. P. Walsh, "A versatile pseudo-random noise generator," *IEEE Trans. Instrum. Meas.*, vol. IM-25, no. 2, pp. 112–116, Jun. 1976.

**Steven A. Owens** received the B.S. degree in physics from U.S. Air Force Academy in 2014 and the M.S. and Ph.D. degrees in engineering physics from the Air Force Institute of Technology (AFIT) in 2016 and 2022, respectively.

**Mark F. Spencer** received the Ph.D. degree in optical sciences and engineering (OSE) from the Air Force Institute of Technology (AFIT) in 2014. He is currently a Directed Energy Staff Specialist with Headquarters U.S. Indo–Pacific Command as the first-ever liaison with the Air Force Research Laboratory, Directed Energy Directorate. He is also an Adjunct Associate Professor in OSE with the Department of Engineering Physics, AFIT. He is also a fellow of SPIE and a Senior Member of *Optica*.

**Glen P. Perram** received the B.S. degree in applied and engineering physics from Cornell University in 1980 and the Ph.D. degree in physics from the Air Force Institute of Technology (AFIT) in 1986. He has been a Professor in physics with AFIT since 1989. He is also a registered Professional Engineer in OH, USA. He is also a fellow of the Directed Energy Professional Society and *Optica*. He received the 2013 Air Force Outstanding Civilian Senior Scientist Award for his work on Diode Pumped Alkali Lasers and the General Bernard A. Schriever Award for Advancing Aerospace Power in 1995.